Stress-driven crystallization via shear-diffusion transformations in a metallic glass at very low temperatures

Yunwei Mao,[1] Ju Li,[1,2,*] Yu-Chieh Lo,[2] Xiaofeng Qian,[2] and Evan Ma[1,3,†]

[1]*Center for Advancing Materials Performance from the Nanoscale, State Key Laboratory for Mechanical Behavior of Materials, Xi'an Jiaotong University, Xi'an 710049, China*

[2]*Department of Nuclear Science and Engineering and Department of Materials Science and Engineering, Massachusetts Institute of Technology, Cambridge, Massachusetts 02139, USA*

[3]*Department of Materials Science and Engineering, Johns Hopkins University, Baltimore, Maryland 21218, USA*

(Received 13 July 2014; revised manuscript received 6 April 2015; published 5 June 2015)

At elevated temperatures, glasses crystallize via thermally activated diffusion. However, metallic glasses can also undergo deformation-induced crystallization at very low temperatures. Here we demonstrate the crystallization of $Al_{50}Fe_{50}$ metallic glasses under cyclic deformation at 50 K using molecular dynamics simulations and reveal the underlying atomic-scale processes. We demonstrate that stress-driven nonaffine atomic rearrangements, or shear diffusion transformation (SDT) events, lead to successive metabasin-to-metabasin transitions and long-range ordering. We also illustrate that the nucleation and growth of the crystal proceed via collective attachment of ordered clusters, advancing the amorphous/crystal interface in an intermittent manner. The cooperative nature of the steplike crystallization is attributed to the large activation volume of Eshelby transformations which generate as a by-product nonaffine diffusive atomic displacements that accumulate over loading cycles. The dual nature of shear (affine) and diffusion (nonaffine) in low-temperature stress-driven SDT events thus unifies inelasticity with crystallization.

DOI: 10.1103/PhysRevB.91.214103 PACS number(s): 64.70.pe, 64.60.Cn, 64.60.qe, 64.70.dg

I. INTRODUCTION

Crystallization, including liquid-to-crystal transition (LCT) and glass-to-crystal transition, is an important process in materials physics. The mechanism of LCT in simple metals is now quite clear [1–3]: a series of monomolecular additions (condensations) to a droplet leads to crystal nucleation in the liquid, mediated by atomic attachments/detachments across the liquid/crystal interface [4]. In crystallization of glasses, most previous work has dealt with thermally induced transitions upon heating of a glass to above its glass-transition temperature [5–7]. Nucleation and growth are again mediated by thermally activated diffusional hops of atoms at the glass/crystal interface.

In recent years, however, it has been proposed that metallic glasses (MGs) may also crystallize at very low temperatures (such as <77 K), if the MG is subjected to shear-dominated deformation [8–10]. This type of crystallization is not thermally induced as the starting temperature is low, and deformation imposed causes little temperature rise [8,11,12]. This mechanical deformation-driven crystallization is in fact ubiquitous in polymers [13], proteins, and alloys [14]. But how the atoms reorganize under externally applied stresses to form crystals in the absence of temperature-induced atomic mobility and what the differences are from thermal-diffusion-mediated crystallization remain largely unresolved. Low-temperature stress-driven *plasticity* of MGs is explained by Argon's shear transformation zone (STZ) model based on Eshelby's solution of sheared ellipsoids [15], including shear banding which can be described as spatially correlated STZ events [16,17]. However crystallization must require nonaffine diffusive reorganization of atoms which seems to be outside of the STZ language.

Here we report a mechanistic study of the crystallization process in an $Al_{50}Fe_{50}$ MG under cyclic loading in molecular dynamics (MD) simulations [12]. A fatigue crack with appropriate geometry under cyclic loading was used, which would not generate a cross-sample large shear band [18] that may create temperature rise [19] and other complications [17,20]. This geometry also gives rise to locations close to the crack tip where the stress is amplified to accelerate the crystallization in local regions within the limited simulation time. Meanwhile, the stress gradient away from the crack ensures an elastic surrounding to conduct away the heat and keeps the local crystallization zone under the isothermal condition and allows stable fatigue cycles to be accrued for easier observation of crystallization in small-scale simulations. Here crystallization was induced by the imposed stress at a very low temperature (50 K). The temperature was so low that conventional models do not apply, such as the diffusion-limited model based on transition rate theory or a collision-limited model [21]. It is the local accumulation of nonaffine displacements with strain cycle that culminates in amorphous-to-crystal transition. In particular, we highlight cooperative behaviors unique to this form of crystal nucleation and growth in an amorphous matrix.

II. SIMULATION DETAILS

MD simulations were conducted using LAMMPS [22] with atomic configurations displayed using ATOMEYE [23]. The atomic interactions in the $Al_{50}Fe_{50}$ alloy were modeled using the embedded atom method potentials by Mendelev *et al.* [24]. A small glass sample consisting of 2000 atoms was prepared from a melting-and-quenching simulation of a random substitutional solid solution in a fcc lattice, which

*liju@mit.edu
†ema@jhu.edu

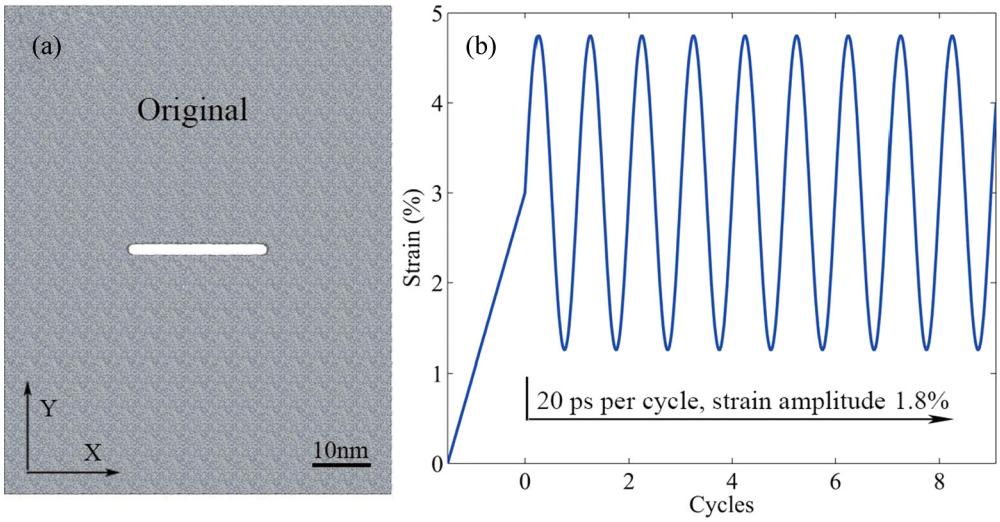

FIG. 1. (Color online) Molecular dynamics simulation setup. (a). Initial sample morphology with a crack. (b) Detailed loading function used in simulation. See text for details.

was heated from 300 to 3000 K, equilibrated for 2 ns, and then cooled down to 50 K at an effective heating and cooling rate of 0.425 K/ps. The time step for integration was 2 fs. Pressure was maintained at zero during both the heating and the cooling processes. A periodic boundary condition was applied to all three directions. The final size of the small sample is $\sim 4 \times 4 \times 2\,\mathrm{nm}^3$. After that, a larger sample with final dimensions of $\sim 59 \times 74 \times 2\,\mathrm{nm}^3$ was produced by duplicating the small sample along the x and y axes. Then a crack of dimensions $\sim 22 \times 2 \times 2\,\mathrm{nm}^3$ was introduced in the center of the sample. Figure 1(a) shows the initial geometry of the sample with dimensions of $\sim 59 \times 74 \times 2\,\mathrm{nm}^3$ and a cracklike notch with dimensions of $22 \times 2 \times 2\,\mathrm{nm}^3$.

The simulation was carried out as follows. We first applied a tensile strain of 3% (below the yield strain of ~5.6% at the strain rate of $\sim 10^9$/s), followed by cyclic loading [with a period of 20 ps and a strain amplitude of 1.8% along the y axis, see Fig. 1(b)]. The strain along the z axis remains zero.

III. RESULTS AND DISCUSSIONS

A. Deformation-induced crystallization

The final morphology after 355 cycles is displayed in Fig. 2(a). The atoms in different environments (characterized using the Honeycutt-Anderson method [25,26]) are highlighted using different colors with blue, green, and maroon representing the bcc-, fcc-, and hcp-like atoms, respectively. Two relatively large crystals, C1 and C2, formed in the sample in regions where the stresses are the highest. The directions of dense-packed planes are marked with "k" in Fig. 2(a). The dense-packed planes of fcc/hcp/bcc are nearly aligned with the directions of the shear stress under this deformation-induced crystallization. This clearly reveals one difference from the case of scalar temperature-induced amorphous-to-crystal transition: the tensorial stress stimuli for crystallization lead to a preferred texture/directionality of the nucleated crystal such that the nucleated crystals tend to have their crystallographic slip planes nearly parallel to the local shear

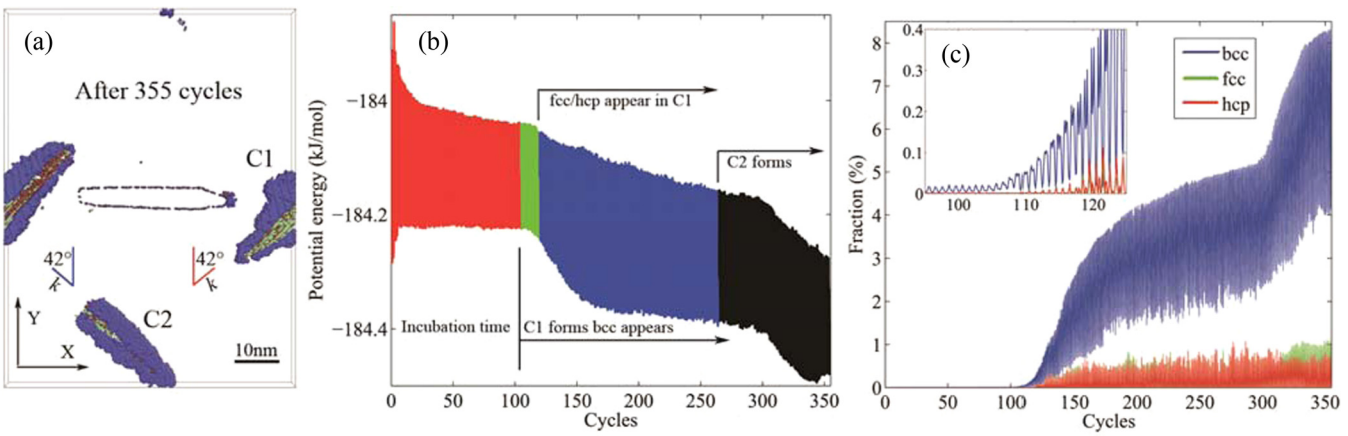

FIG. 2. (Color online) Molecular dynamics simulation of the cyclic-straining-induced crystallization in $Al_{50}Fe_{50}$ metallic glass. (a). Final morphology after 355 cycles. Two crystals (C1 and C2) form. (b) Potential energy versus loading cycles, showing obvious energy reduction during glass-crystal transition. (c). Fraction of crystal-like atoms versus cycles.

stress direction. The other basic difference from the LCT is that a liquid state is at equilibrium, whereas our glass is out of equilibrium (nonergodic) to start with, and with the application of large stress it potentially may step further away from equilibrium (rejuvenation). Instead, the cyclic stress here helps our simulation system approach the true energy minimum, the crystalline state.

The potential energy of the whole system, including the atoms involved in crystallization and those that remained amorphous, is plotted as a function of cycle numbers in Fig. 2(b). The corresponding rise of the fraction of crystallized atoms is shown in Fig. 2(c). The crystallization process includes several stages: (1) an incubation period with almost constant potential energy (cycle $<$ 105). In this stage crystal-like atoms appear randomly but cannot be stabilized with no net sustained fraction in Fig. 2(c); (2) a short period where the expected bcc phase (C1) nucleates [see the rapidly rising fraction of bcc atoms in Fig. 2(c)], sharply decreasing the potential energy (105 $<$ cycle $<$ 125); (3) the fraction of bcc atoms continues to rise, together with a small fraction of fcc/hcp-like atoms (which emerge due to shear-induced bcc-fcc transformation) in the growing C1 crystal. The growth of the C1 crystal continuously reduces the potential energy (125 $<$ cycle $<$ 170). For cycle $>$ 265, another bcc crystal C2 nucleates, similar to the case of C1.

B. Atomistic mechanism during the incubation period

During the incubation period, structural adjustments/relaxations result in some atoms with enhanced local order. The "ordered atoms" have a higher degree of short-to-medium range order relative to those in the glassy matrix; their high degree of rotational symmetry is quantified by the order parameters Q_6 and C_6 [3,27,28], respectively.

We characterize the local structure around atom i by a set of numbers $q_{lm}(i)$ which defined as

$$q_{lm}(i) = \frac{1}{N_i} \sum_{j \in N_i} Y_l^m(\widehat{r_{ij}}), \tag{1}$$

where $Y_l^m(\widehat{r_{ij}})$ are spherical harmonics, $\widehat{r_{ij}}$ is a unit vector connecting atom i and its neighbor j, and the sum runs over all N_i neighbors of particle i. A global bond rotational invariant $Q_l(i)$ of atom i, is constructed from $q_{lm}(i)$ by

$$Q_l(i) = \left[\frac{4\pi}{2l+1} \sum_{m=-l}^{l} |q_{lm}(i)|^2 \right]^{1/2}. \tag{2}$$

Also, we define the connection number of atom i as

$$C_l(i) = \sum_{j \in N_i} H(S_l(i,j) - S_{\text{thre}}), \tag{3}$$

where $H(x)$ is the step function. $S_l(i,j) = |\sum_{m=-l}^{l} \tilde{q}_{lm}(i)\tilde{q}^{\star}_{lm}(j)|$ is the connecting parameter to judge whether atom i and its neighbor j is connected [28], and S_{thre} is a threshold value set as 0.28 in our case. Here $\tilde{q}_{lm}(i)$ is the normalized $q_{lm}(i)$ which reads $\tilde{q}_{lm}(i) = q_{lm}(i)/|q_{lm}(i)|$. For both parameters $Q_l(i)$ and $C_l(i)$, we set $l = 6$.

Atoms with high $C_6(C_6 > 10)$ value are called ordered atoms here. Figure 3 shows the details of structural relaxations

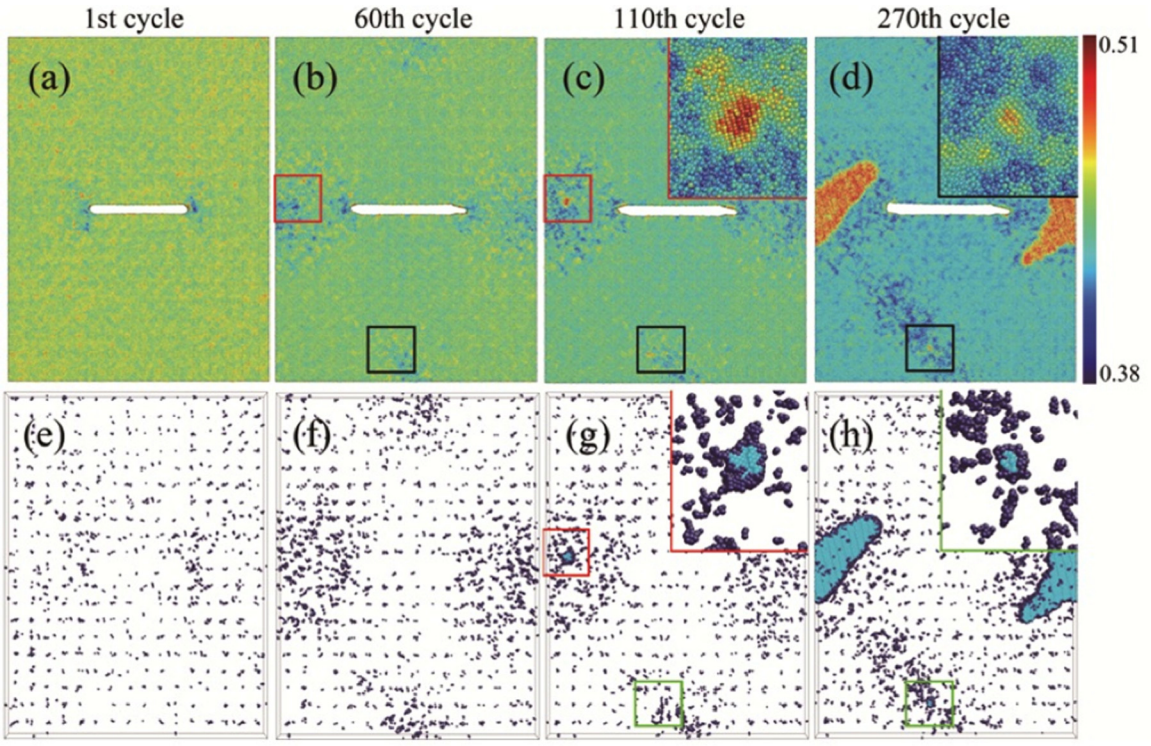

FIG. 3. (Color online) Structural relaxations within incubation time. (a)–(d) give the distribution of order parameter Q_6 in the 1st, 60th,110th, and 270th cycles. (e)–(h) give the distribution of ordered atoms in corresponding cycles. The boxes in these figures highlight some active zones with a high content of ordered atoms, and close-up views are shown in the insets.

during the incubation stage for the atoms involved in crystals C1 and C2. Figures 3(a)–3(d) show the distribution of order parameter Q_6 in the 1st, 60th, 110th, and 270th cycles, respectively. Initially the order parameter is almost random in the whole sample. With increasing cycles, certain areas highlighted by red and black frames become more ordered and eventually result in nucleation of C1 and C2 [see the insets in Figs. 3(c) and 3(d)]. Furthermore, Figs. 3(e)–3(h) display the corresponding distributions of ordered atoms using connection number C_6 at the same cycle of Figs. 3(a)–3(d). As the cycle goes on, the number of ordered atoms in active zones (zones with lower Q_6 than surroundings) increases, and these atoms form small clusters. The red and green frames highlight these changes. When these ordered clusters form, they are reshaped by the loading-induced stress/strain, some of them even grow up, leading to crystal nucleation [see the insets of Figs. 3(g) and 3(h), the light-blue atoms are crystal-like whereas the dark blue are deformation-induced ordered].

C. Atomistic mechanics during nucleation

Next, our focus is to uncover the details of the atomic-level processes that mediate crystallization. To this end, the C2 formation, which has a long incubation period (see Fig. 2) is analyzed in Fig. 4. An example is the 52-atom supercluster in Fig. 4. These distributed atoms then merge together later in a "jump" that nucleates the C2 crystal. In other words, clusters of ordered atoms cooperate to assemble into the nucleating crystal.

To confirm that this nucleation is temporally intermittent, we use a "distance matrix" (DM) [29,30] to quantitatively assess the cooperative behavior of the 52-atom supercluster depicted in Fig. 4,

$$\Delta^2(t',t'') = \frac{1}{N}\sum_{i=1}^{N} |\boldsymbol{r}_i(t') - \boldsymbol{r}_i(t'')|^2, \tag{4}$$

where $\boldsymbol{r}_i(t)$ is the position of particle i at time t. Figure 4(d) shows the DM of this supercluster as a function of two time arguments t' and t'' with darker compartments along the diagonal corresponding to the configurations that are within a small distance (DM) relative to one another. We observe that the dynamics of the supercluster is quite temporally intermittent: It stays in a local configuration space (i.e., a metabasin, defined as a set of configurations that make more frequent transitions between each other than with others [31,32]) for a rather long period of time before it finds a pathway to jump into a new metabasin some distance (DM) away. A typical sojourn time within one metabasin is around 20–40 cycles, i.e., 400–800 ps in our case. Figure 4(e) shows $\delta^2(t,\theta)$, the particle averaged squared displacement (ASD) of the supercluster within a time interval θ. This function is defined as $\delta^2(t,\theta) = \Delta^2(t-\frac{\theta}{2}, t+\frac{\theta}{2})$ Å^2 [30]. Here we choose $\theta = 15$ cycles. The selected $\theta = 15$ cycles is considerably longer than the time period of microscopic vibrations but sufficiently shorter than the α-relaxation time (the characteristic time-scale that a major configuration transformation happens [29,30], or the 20–40 cycle size of dark squares along the diagonal). The ASD exhibits clear jumps corresponding to the hopping between metabasins in Fig. 4(d). We conclude that the nucleation of the crystal is due to the collaborative reorganization of many atoms (e.g., the 52 atoms in Fig. 4). Statistically, the supercluster involving atoms undergoing increasing ordering is observed to explore three to six metabasins before finally jumping into the crystal basin. The stress/strain serves as perturbations to trigger the metabasin-metabasin hops of this supercluster, relaxing the atoms involved into their more and more favorable configurations. This eventually ends with a collaborative action of all the atoms in and immediately next to the supercluster, directed/aligned by applied stresses, in establishing the crystal with translational symmetry. These features are quite different from that in the LCT where thermally activated diffusion of individual atoms is the dominant mediating process.

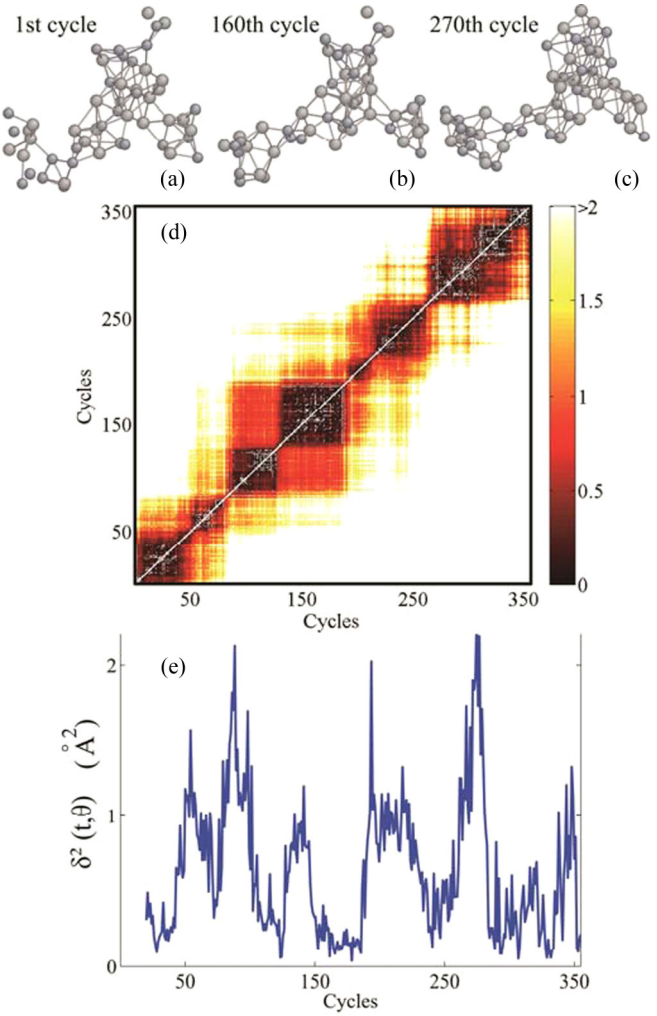

FIG. 4. (Color online) Atomic configuration during the formation of C2 and cooperative behavior of this cluster. The distributed 52 atoms in (a) are gradually assembled into more ordered packing [(b) through (c)] due to the accumulation of nonaffine displacements under cyclic deformation. (d) shows DM for the cluster in (a). (e) ASD for the trajectory in (d). The value of θ in $\delta^2(t,\theta)$ is 15 periods.

D. Atomistic mechanics during growth

The crystal then grows (the crystallization is preferentially in the nucleated regions where stresses are larger than in

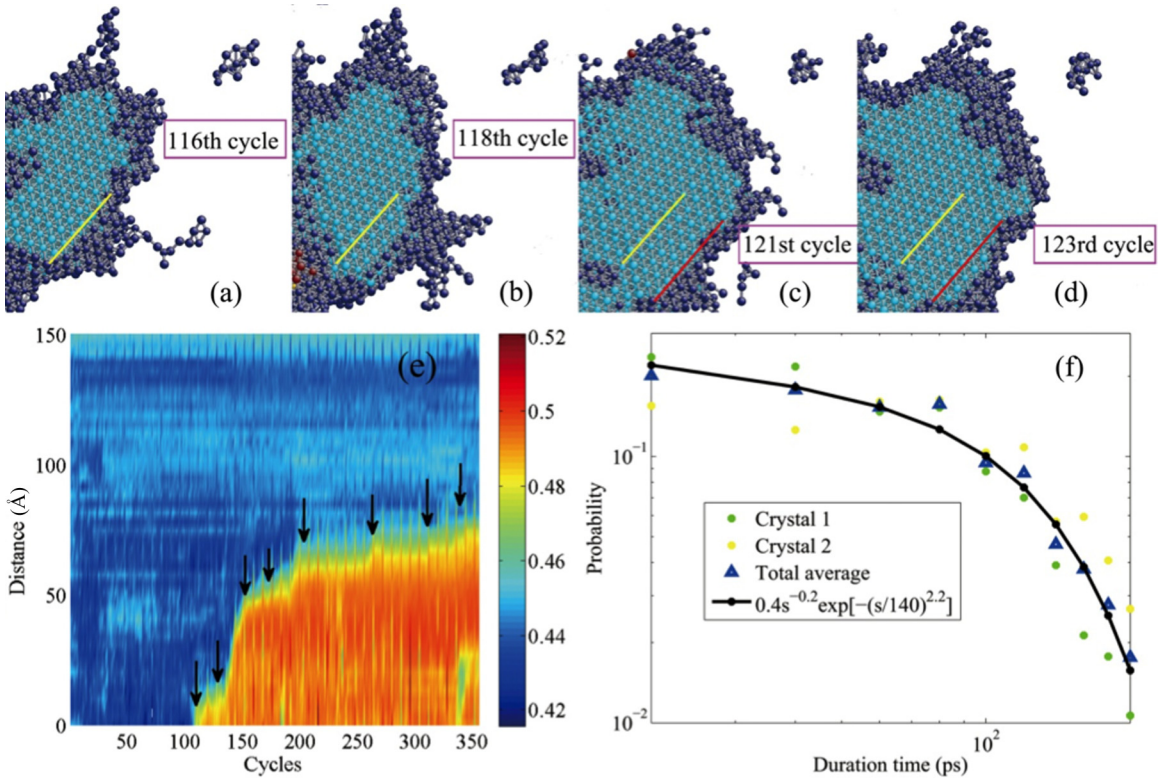

FIG. 5. (Color online) Cooperative behavior during the growth of crystal C1 in the MG matrix. (a)–(d) show the evolution of the crystal/amorphous interface after 116, 118, 121, and 123 cycles. The ordered atoms (dark blue) transform into crystal, and the corresponding interface moves outwards within two cycles as indicated by the position of the yellow line in (b), whereas the interface moves less from (c) to (d). (e) A typical example showing the motion of the interface at different times (cycles). The different colors rank the atomic order parameter Q_6 of the atoms. High values in the Q_6 order parameter represent ordered/crystal-like atoms whereas low values correspond to the glass matrix. Black arrows mark the intermittent jumps of the interface position, corresponding to the jerky and collective advancements of the interface. (f) Probability of the wait duration time for interface jump (in a double-log plot). The data are fitted by a power law multiplied by a stretched exponential $P = 0.4s^{-0.2}\exp[-(s/140)^{2.2}]$.

other areas). Figure 5 monitors the growth of the C1 crystal at various time intervals (in the 116th, 118th, 121st, and 123rd cycles, respectively). Here the dark blue atoms are the ordered atoms, again quantified by the order parameters Q_6 and C_6 [3,27,28]. The atoms colored in light blue represent crystal atoms (here we do not show the bcc/fcc/hcp atoms separately; all of them are colored in light blue). We find that the growing crystal is always preceded by ordered atoms (dark blue) forming an encapsulating layer at the interface. This layer is formed by absorbing nearby small clusters of ordered atoms. The yellow and red lines in Figs. 5(a)–5(d) highlight the advancement of one interface. From the 116th cycle to the 118th cycle, the interface marches forward rapidly (three layers for two periods), but in the ensuing 118th–123rd cycles, the interface grows slowly (two layers for five periods). This is an example indicating that the growth is also temporally intermittent, similar to the jerky basin hopping observed in the nucleation process (Fig. 4). Figure 5(e) shows the position (distance relative to its original location) of one particular interface as a typical example at different times (cycles).The different colors rank the atomic order parameter Q_6 of the atoms. High values in the Q_6 order parameter represent ordered/crystal atoms (green: encapsulating layer/red: the growing crystal) whereas low values correspond to the glass matrix (blue region). Black arrows in Fig. 5(e) mark the moments at which intermittent jumps occur, corresponding to the collective advancements of the interface. The crystal grows during some cycles [see the range of jump distances in Fig. 5(e)] and stops in some others. The probability of growth, along various directions, is presented in Fig. 5(f) as a function of the wait time between the growth bursts. We use a power law $P = fs^{-\Delta}\exp[-(s/t_0)^{\eta}]$ [33] to fit the data, where s is the wait time between two successive growth bursts in Fig. 3(e) and (f, Δ, t_0,η) are four fitted parameters. The fit gives $f = 0.4$, $\Delta = 0.2$, $t_0 = 140$ ps (seven cycles), and $\eta = 2.2$. Note the cutoff t_0 at seven cycles, which represents that almost all crystal/glass interfaces will march within seven cycles. This is at the same order of magnitude with that in experiment (in our experiments [12], within ~1000 cycles, the crystal grows into a nanograin with a diameter of 30 nm (~100 crystalline planes), then roughly ten cycles is needed to advance the crystal/glass interface). The curve clearly shows that the growth is intermittent and collective. The 140-ps (seven cycles) cutoff means that the wait time rarely exceeds 140 ps (seven cycles). Therefore 140 ps (seven cycles) is a characteristic time scale for this cooperative growth.

E. Differences between the LCT and the deformation-induced crystallization

To compare with the crystal growth in the LCT, a (37 × 37 × 2)-nm $Al_{50}Fe_{50}$ sample of 200 000 atoms was cooled at a rate of 0.07 K/ps from liquid melt at 2000 K. Two crystals nucleate at ∼1050 K, followed by rapid growth. As seen in Fig. 6, for crystal growth from liquid at this temperature, the fitted characteristic cutoff t_0 is only 12 ps. Moreover, the exponent η in the exponential tail of this distribution is 3.0, indicative of a faster process. The curve in Fig. 6 is now shifted to the left by one order of magnitude in time, and the interface moves almost continuously with a wait time of only a few picoseconds. This can thus be perceived as a process via diffusive actions of *individual* atoms, just as in classical nucleation theory.

We next explain why the crystal formation requires cooperative actions in bursts. At a temperature far below T_g, thermal diffusion of atoms is suppressed such that individual atoms do not have the mobility to search for low-energy locations by switching positions to join the incipient/growing crystal. Instead, small groups of atoms are agitated under tensorial stress to undergo shear-diffusion transformations (SDT),

$$\mathbf{d}_{ji} \equiv \mathbf{d}^0_{ji}\mathbf{J}_i + \mathbf{s}_{ji}, \quad D_i^2 \equiv \min_{\mathbf{J}_i} \frac{1}{N_i} \sum_{j\in N_i} |\mathbf{s}_{ji}|^2, \quad j \in N_i, \qquad (5)$$

where $j \in N_i$ are atom i's original nearest neighbors and $\mathbf{d}_{ji}$ and $\mathbf{d}^0_{ji}$ are the present and original distance vectors between atom i and its original neighbor j. $\mathbf{J}_i$ is a 3 × 3 matrix defined on each atom i, that is optimized for given sets of $\{\mathbf{d}^0_{ji}\}$ and $\{\mathbf{d}_{ji}\}$ to minimize the local diffusion part D_i^2, constituting nonaffine displacement $\mathbf{s}_{ji}$ of each neighbor [19,34]. In essence, Eq. (5) is an atomistic affine/nonaffine decomposition, that seeks the best affine matrix connecting $\{\mathbf{d}^0_{ji}\}\rightarrow\{\mathbf{d}_{ji}\}$ while acknowledging that nonaffine or diffusive displacements may still exist as the residual displacements on top of that. Although individual SDTs are akin to β-relaxation events, the accumulation of the nonaffine displacements $\mathbf{s}_{ji}$ along the cyclic loading process by these SDT events plays the role of diffusion [12] to allow the atoms to develop more local order and gradually look for more comfortable configurations. Along the way towards the eventual crystal configurations, there are intermittent collective hopping events from metabasin to metabasin (akin to α relaxation in steps) as discussed earlier. The collectivity of SDT events is characterized by the activation volume Ω, which is proportional to the number of atoms that simultaneously break their bonds at the saddle point [35] in a metabasin-to-metabasin transition. For purely temperature-driven LCT, the activation volume Ω involves one or a few atoms in simple metals. But for the low-temperature stress-driven SDT process discussed here, Ω involves many tens or even hundreds of atoms as illustrated by the MD data.

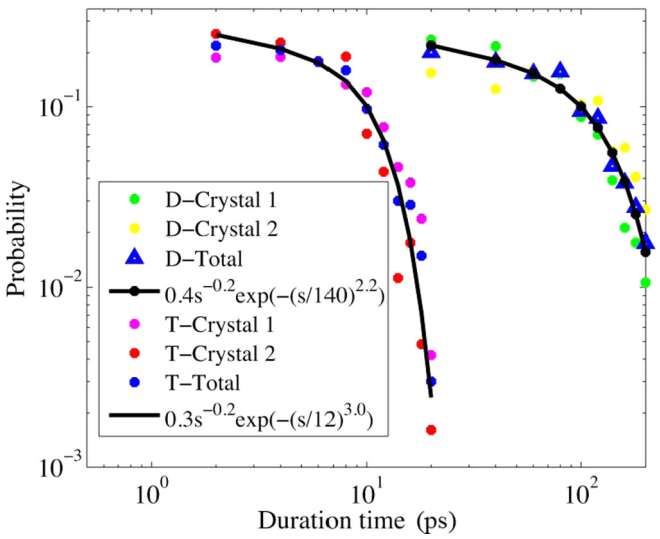

FIG. 6. (Color online) The advancement of crystal/amorphous interfaces, comparing temperature-induced (T-crystal 1 and T-crystal 2) versus deformation-induced (D-crystal 1 and D-crystal 2) crystallization. D/T total is for the sum of the two crystals. Black lines are guides to the eye.

In Eq. (5) the non-negative D_i^2 quantity is meant to be the parallel of mean-squared displacement (MSD) in thermally driven diffusion, even though it is mainly stress driven. The defining characteristic of MSD in thermally driven diffusion is its linear growth with time. Here, D_i^2 accumulates approximately linearly with the cycle number. With sufficient order accumulated collectively among the atoms involved in the group, the supercluster becomes "ready" to be pushed at the next moment (a bit more straining) into the crystal configuration, joining and expanding the crystal. Although the minimal glass-to-crystal distance, defined here to be the minimal nonaffine displacement per atom necessary to reorder a disordered system into crystal, is as small as a few angstroms [12], the energy barriers are too high at low temperatures if stress is not applied. A shear-dominant tensorial stress τ lowers the barrier Q significantly [21,36]. Indeed, the activation volume-tensor Ω is defined by how sensitive Q is to stress: $\Omega \equiv -\partial Q/\partial\tau$ [35], and a large activation volume means the barrier $Q(\tau)$ comes down quickly with increasing shear stress applied [17,20,35]. With Q lowered, "menu options" pop up to allow the local configurations to be nudged towards lower-energy valleys. As a result, along with the SDT-mediated ordering (e.g., rising Q_6) the glass undergoes the step-by-step metabasin-to-metabasin transitions to overcome the phase-space distance to the crystal on the potential-energy landscape. The patches of "ready-to-crystallize" atoms do not migrate in the absence of temperature-induced atomic mobility, so the advancing crystal has to wait for more of them to accumulate and link up right at the interface between the glass and the crystal [dark blue regions in Figs. 3(g) and 3(h)].Through this stage, the precursors have incubated to the point that the barrier to reach the crystal becomes sufficiently small. Only then can they be collectively realigned to join the crystal by the stresses in ensuing deformation (readily falling into the crystal basin nearby). This precursor requirement extends the wait time to at least one order of magnitude longer than that in the LCT (Fig. 6), making the interface advancement an intermittent process.

IV. CONCLUSIONS

To recapitulate, our MD simulations reveal that in the absence of temperature-induced thermal diffusion of individual

atoms [37], deformation-driven crystallization at very low temperatures is accomplished in cooperative steps. We find that both the crystal nucleation and the growth are temporally heterogeneous, exhibiting intermittent interface migration. For this new mode of crystallization, the highly cooperative nature is rooted in the larger activation volume Ω and the need to wait, i.e., to get ready (the glass in front of the crystal/glass interface needs to incubate to accumulate local ordering to approach the crystal basin), which can only be accrued over a period of time (e.g., strain cycles here) for a collection of atoms through repeated nonaffine displacements over a series of loading cycles. Such fatigue loading indeed makes the observation of low-T crystallization easier since D_i^2 accrues approximately linearly with cycle number, whereas $\mathbf{J}_i$ oscillates but does not accumulate much; whereas in a monotonic loading to failure (fracture) setup, $\mathbf{J}_i$ accumulates, but D_i^2 does not have enough time to accrue. Thus fatigue loading enhances the diffusion-to-shear (nonaffine-to-affine) ratio of successive shear-diffusion transformation events, making the low-T crystallization easier to simulate and study experimentally [12]. Crystallization via SDT is a low-temperature stress-driven larger-activation-volume process when compared to the LCT. SDT has the dual nature of shear and diffusion, which is mathematically defined by an affine/nonaffine decomposition of relative atomic displacements. As such, SDT is an extension of Argon and Eshelby's shear transformation concept [15,16] which emphasized the affine (shape change) part of stress-driven processes [17,20]. Previously, Delogu [38,39] and Fujita *et al.* [40] have also highlighted nonaffine displacements. Such nonaffine displacements, resulting in local diffusion, could change the initial atomic configuration of the system and eventually induce a disorder-order transition. With the diffusional contribution now properly defined, SDT can be used to explain not only the deformation strains, but also the low-temperature crystallization in a metallic glass [8,12,15]. Finally, we note that solute partitioning is not observed in our experiment [12] or MD simulation as the crystals formed has the same chemical composition as the glass ("massive transformation"), so only short-range diffusion is necessary. In cases where a glass transforms to crystals (or even amorphous phases) with two or more different chemistries, solute partitioning and long-range diffusion have to occur. However, based on what we know about how D_i^2 accumulates with the number of SDT events, we predict that long-range diffusion and solute partitioning can also happen with stress-driven SDTs.

ACKNOWLEDGEMENTS

This work was supported, in part, by the 973 Program of China (Grant No. 2012CB619402). We also appreciate the support from the 111 Project of China (Grant No. B06025). Both J.L. and E.M. benefited from adjunct professorships at XJTU. Y.-C.L., X.Q. and J.L. acknowledge support by NSF Grants No. DMR-1120901 and No. DMR-1410636. E.M. was supported at JHU by the U.S.-DOE-BES, Division of Materials Sciences and Engineering, under Contract No. DE-FG02-09ER46056.

[1] D. Turnbull, Contemp. Phys. **10**, 473 (1969).
[2] P. G. Debenedetti, *Metastable Liquids: Concepts and Principles* (Princeton University Press, Princeton, 1996).
[3] T. Kawasaki and H. Tanaka, Proc. Natl. Acad. Sci. U.S.A. **107**, 14036 (2010).
[4] C. Angell, D. MacFarlane, and M. Oguni, Ann. N.Y. Acad. Sci. **484**, 241 (1986).
[5] X. Liu, G. Chen, H. Hou, X. Hui, K. Yao, Z. Lu, and C. Liu, Acta Mater. **56**, 2760 (2008).
[6] R. Kakkad, J. Smith, W. Lau, S. Fonash, and R. Kerns, J. Appl. Phys. **65**, 2069 (1989).
[7] V. E. Borisenko and P. J. Hesketh, in *Rapid Thermal Processing of Semiconductors*, Microdevices Physics and Fabrication Technologies, Series edited by I. Brodie and A. Sher (Plenum, New York, 1997).
[8] J. J. Kim, Y. Choi, S. Suresh, and A. Argon, Science **295**, 654 (2002).
[9] A. Kawashima, Z. Yuqiao, X. Guoqiang, N. Nishiyama, and A. Inoue, Mater. Sci. Eng., A **528**, 391 (2010).
[10] F. Méar, B. Doisneau, A. Yavari, and A. Greer, J. Alloys Compd. **483**, 256 (2009).
[11] B. Huang, R. Perez, P. Crawford, A. Sharif, S. Nutt, and E. Lavernia, Nanostruct. Mater. **5**, 545 (1995).
[12] C.-C. Wang, Y.-W. Mao, Z.-W. Shan, M. Dao, J. Li, J. Sun, E. Ma, and S. Suresh, Proc. Natl. Acad. Sci. U.S.A. **110**, 19725 (2013).
[13] Y. Ogino, H. Fukushima, N. Takahashi, G. Matsuba, K. Nishida, and T. Kanaya, Macromolecules **39**, 7617 (2006).
[14] K. Kelton and A. L. Greer, *Nucleation in Condensed Matter: Applications in Materials and Biology*, Pergamon Materials Series (Pergamon, Oxford, 2010).
[15] A. Argon, Acta Metall. **27**, 47 (1979).
[16] C. A. Schuh, T. C. Hufnagel, and U. Ramamurty, Acta Mater. **55**, 4067 (2007).
[17] P. Zhao, J. Li, and Y. Wang, Acta Mater. **73**, 149 (2014).
[18] A. Greer, Y. Cheng, and E. Ma, Mater. Sci. Eng., R **74**, 71 (2013).
[19] F. Shimizu, S. Ogata, and J. Li, Mater. Trans. **48**, 2923 (2007).
[20] P. Zhao, J. Li, and Y. Wang, Int. J. Plast. **40**, 1 (2013).
[21] Y. Ashkenazy and R. Averback, Acta Mater. **58**, 524 (2010).
[22] S. Plimpton, J. Comput. Phys. **117**, 1 (1995).
[23] J. Li, Modell. Simul. Mater. Sci. Eng. **11**, 173 (2003).
[24] M. Mendelev, D. Srolovitz, G. Ackland, and S. Han, J. Mater. Res. **20**, 208 (2005).
[25] J. D. Honeycutt and H. C. Andersen, J. Phys. Chem. **91**, 4950 (1987).
[26] H. Tsuzuki, P. S. Branicio, and J. P. Rino, Comput. Phys. Commun. **177**, 518 (2007).
[27] P. J. Steinhardt, D. R. Nelson, and M. Ronchetti, Phys. Rev. B **28**, 784 (1983).
[28] P. R. Ten Wolde, M. J. Ruiz-Montero, and D. Frenkel, Phys. Rev. Lett. **75**, 2714 (1995).
[29] I. Ohmine, J. Phys. Chem. **99**, 6767 (1995).
[30] G. Appignanesi, J. Rodriguez Fris, R. Montani, and W. Kob, Phys. Rev. Lett. **96**, 057801 (2006).
[31] A. Heuer, J. Phys.: Condens. Matter **20**, 373101 (2008).

[32] J. C. Mauro, R. J. Loucks, and P. K. Gupta, J. Phys. Chem. A **111**, 7957 (2007).
[33] F. F. Csikor, C. Motz, D. Weygand, M. Zaiser, and S. Zapperi, Science **318**, 251 (2007).
[34] M. Falk and J. Langer, Phys. Rev. E **57**, 7192 (1998).
[35] J. Li, MRS Bull. **32**, 151 (2007).
[36] D. J. Lacks and M. J. Osborne, Phys. Rev. Lett. **93**, 255501 (2004).
[37] S. W. Nam *et al.*, Science **336**, 1561 (2012).
[38] F. Delogu, Intermetallics **19**, 86 (2011).
[39] F. Delogu, Mater. Chem. Phys. **126**, 152 (2011).
[40] T. Fujita, Z. Wang, Y. Liu, H. Sheng, W. Wang, and M. Chen, Acta Mater. **60**, 3741 (2012).